

TinySense: Effective CSI Compression for Scalable and Accurate Wi-Fi Sensing

Toan Gian*, Dung T. Tran*, Viet Quoc Pham[†], Francesco Restuccia[†], and Van-Dinh Nguyen*[‡]

*Smart Green Transformation Center (GREEN-X), VinUniversity, Hanoi, Vietnam

[†]Department of Electrical & Computer Engineering, Northeastern University, MA, USA

[‡]School of Computer Science and Statistics, Trinity College Dublin, Ireland (dinh.nguyen@tcd.ie)

Abstract—With the growing demand for device-free and privacy-preserving sensing solutions, Wi-Fi sensing has emerged as a promising approach for human pose estimation (HPE). However, existing methods often process vast amounts of channel state information (CSI) data directly, ultimately straining networking resources. This paper introduces TinySense, an efficient compression framework that enhances the scalability of Wi-Fi-based human sensing. Our approach is based on a new vector quantization-based generative adversarial network (VQ-GAN). Specifically, by leveraging a VQGAN-learned codebook, TinySense significantly reduces CSI data while maintaining the accuracy required for reliable HPE. To optimize compression, we employ the K-means algorithm to dynamically adjust compression bitrates to cluster a large-scale pre-trained codebook into smaller subsets. Furthermore, a Transformer model is incorporated to mitigate bitrate loss, enhancing robustness in unreliable networking conditions. We prototype TinySense on an experimental testbed using Jetson Nano and Raspberry Pi to measure latency and network resource use. Extensive results demonstrate that TinySense significantly outperforms state-of-the-art compression schemes, achieving up to $1.5\times$ higher HPE accuracy score (PCK₂₀) under the same compression rate. It also reduces latency and networking overhead, respectively, by up to $5\times$ and $2.5\times$. The code repository is available online at [here](https://github.com/ToanGian/TinySense).

I. INTRODUCTION

Motivation. Wi-Fi-based sensing has recently attracted significant interest within the research community due to its cost-effectiveness, extensive infrastructure, and non-intrusive nature [1]–[3]. Critically, Wi-Fi sensing relies on the effective and efficient measurement of channel state information (CSI) [4], which captures the detailed signal propagation characteristics between transmitting and receiving antennas over multiple subcarriers. This data enables device-free localization [1], human activity recognition (HAR) [2], gesture recognition [3] and human pose estimation (HPE) [5], [6].

Recent studies have investigated the integration of deep learning (DL) into Wi-Fi sensing-based HPE tasks. For instance, MetaFi++ [7] introduced a Transformer-based approach, and PerUnet [6] utilized Unet architecture enhanced with attention mechanisms to address HPE challenges. Additionally, WiPose [8] tackled occluded and cross-domain scenarios by applying extensive pre-processing to Wi-Fi sensing data and leveraging recurrent neural networks (RNNs) for

The first two authors contributed equally to this work. V.-D. Nguyen carried out his contribution while affiliated with VinUniversity. This work is sponsored by VinUniversity under Grant No. VUNI.GT.NTKH.06.

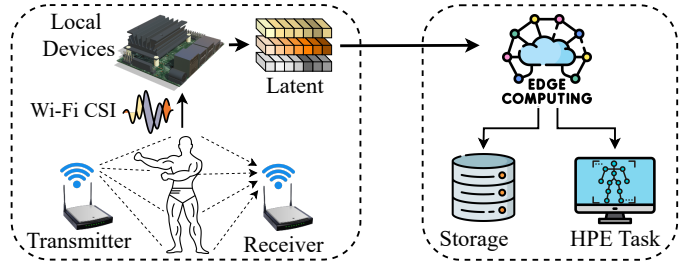


Fig. 1: Overview of Cloud-based Wi-Fi Sensing.

improved performance. Meanwhile, AdaPose [9] introduces a mapping-consistency loss that mitigates domain discrepancies between source and target domains. In parallel, PiW-3D [10] represents a pioneering Wi-Fi-based system capable of achieving multi-person 3D pose estimation. For a recent survey on the topic, please refer to the excellent work.

Existing limitations. Existing approaches demand substantial computational resources, limiting their practicality in real-world deployments. For example, running large neural networks locally for Wi-Fi sensing is infeasible on resource-constrained devices, with models reaching up to 26.42 million parameters [7]. While offloading CSI processing to cloud servers alleviates computation constraints, the extremely high dimensionality and sampling rate of CSI introduce severe communication overhead. Under Wi-Fi 7 at full physical (PHY) bandwidth (*i.e.*, 320 MHz, 3920 subcarriers, and 16 spatial streams), each CSI report reaches 4.014 MB; at a sampling rate of 500 Hz [7], this results in nearly 2 GB/s of traffic, potentially saturating Wi-Fi networks. Classical compression methods [11]–[13] are ineffective due to their linear assumptions, which fail to capture the complex frequency-temporal correlations induced by human motion. Moreover, recent learning-based approaches often overlook the joint optimization of compression rate and sensing accuracy [14], [15], still incurring significant bandwidth costs. For instance, [16] requires 7.5 Kb/s for CSI transmission, while [14], despite high compression, reports limited reconstruction quality (norm mean square error (NMSE) of -3.28 dB). As a result, scalability and efficiency remain unresolved challenges [15].

Key contributions. We propose TinySense to perform high CSI compression rates while maintaining high-quality CSI reconstruction without significant loss in HPE performance.

As shown in Fig. 1, the core idea is to partition the large DNN of an HPE-enabled device into a lightweight *local* DNN, deployed on each mobile device, and a *global* DNN, executed at the nearest server. The local DNN transforms CSI data into a “*compressed*” latent representation based on a vector quantization-based generative adversarial network (VQGAN) [17], thus decreasing networking overhead while retaining high-quality CSI reconstruction and accurate HPE. We further apply K-means clustering to enable a large pre-trained codebook, thus creating a set of smaller codebooks that represent CSI data through different VQ index maps, thus allowing flexible bitrate and reconstruction quality. To mitigate bitstream loss in unstable transmission conditions, we leverage VQGAN’s second-stage transformer to predict missing indices based on the underlying discrete distribution, thus effectively preventing reconstruction failures.

Summary of the main contributions

- We propose TinySense to perform high-quality CSI reconstruction and accurate HPE while achieving ultra-low bitrate compression through the shared codebook learning capability of the VQGAN architecture. Our approach partitions the large DNN between the local device and the cloud server, while compressing the CSI data into a compact latent representation to transmit. This design substantially reduces both computational demands and networking overhead.
- We develop a K-means clustering method to reduce the large codebook into smaller versions, enabling variable bitrates and adaptive reconstruction quality. Our work takes a new step towards proposing a second-stage Transformer to predict missing indices that help enhance model robustness by mitigating bit loss in challenging network conditions.
- We prototype TinySense on an experimental testbed consisting of a Raspberry PI/Jetson Nano and an RTX 8000 GPU acting as a mobile device and edge server, respectively, to measure the end-to-end latency and networking overhead. Experimental results indicate that TinySense reduces the communication burdens by over 1,700 times without reducing the HPE performance. In addition, we significantly outperform state-of-the-art (SOTA) compression schemes [14], [15] by achieving 1.25 and 1.5 times higher PCK_{20} scores than EfficientFi [14] and RSCNet [15], respectively, under the same compression rate. It also reduces latency and bandwidth by up to 5× and 2.5× compared to EfficientFi [16].

Paper organization. Section II reviews related work, and Section III provides the necessary background. Section IV presents the TinySense framework, while Section V evaluates its performance. Finally, Section VI concludes the paper.

II. RELATED WORK

Wi-Fi-based HPE tasks. Wi-Fi infrastructure combined with open-source tools has sparked interest in using CSI for human sensing. Numerous studies (*e.g.* [5], [8], [18]) aim to improve

TABLE I: Comparison of CSI Feedback and Sensing Methods

Method	Core Technique	Task-Aware	Adaptive Bitrate	Robustness
LASSO / PCA [11]–[13]	Linear/ Sparse Recovery	No	No	Low
CSINet [24]	CNN Autoencoder	No	No	Low
EfficientFi [14]	VQ-VAE	Partial	No (Fixed Codebook)	Low
RSCNet [15]	CNN	Yes	Yes (Dynamic)	Low
TinySense (Ours)	VQGAN + Transformer	Yes	Yes (K-means)	High (Transformer)

Wi-Fi-based HPE accuracy using off-the-shelf devices, balancing cost-effectiveness and the limitation of low subcarrier counts. MetaFi [19] and its variants [7] addressed this by enhancing subcarrier resolution to 114 subcarriers, though the resulting high-dimensional CSI data increases transmission overhead. Very recently, [20]–[23] proposed lightweight models to accelerate inference while maintaining high accuracy. However, these designs can still be impractical for edge devices with limited compute and power budgets, and they do not address the communication burden inherent to edge–server architectures. This underscores the need for efficient CSI compression prior to cloud transmission. Our approach introduces a novel method for compressing and transmitting CSI data to improve cloud-based HPE processing.

CSI data compression. Efficient CSI compression is crucial for reducing communication overhead in cloud-based Wi-Fi sensing, as CSI is inherently high-dimensional. Traditional linear methods [11]–[13] exploit sparsity but fail to capture the non-linear frequency–temporal characteristics critical for HPE. DL-based approaches such as CSINet [24] improve reconstruction accuracy but primarily optimize signal fidelity rather than preserving high-level semantic features for sensing. EfficientFi [14] adopts VQ-VAE with a fixed codebook, limiting bitrate adaptability under dynamic bandwidth conditions, while RSCNet [15] targets real-time operation but lacks robustness to packet loss common in edge computing. In contrast, TinySense leverages VQ-GAN for task-aware CSI compression, enabling strong downstream performance with low reconstruction error. Moreover, K-means–based codebook resizing supports adaptive bitrate control, and a Transformer-based recovery module improves robustness under constrained network conditions. A systematic comparison is provided in Table I.

III. BACKGROUND

A. Channel State Information

CSI captures fine-grained information about the wireless transmission channel, reflecting environmental characteristics and human motion through multipath propagation and signal reflections. Modern IEEE 802.11 Wi-Fi systems employ Orthogonal Frequency-Division Multiplexing (OFDM) and multiple antennas, enabling CSI to record amplitude attenuation and phase shifts across subcarriers and antenna pairs. By

representing the channel in the frequency domain, CSI supports precise modeling and analysis of wireless propagation, commonly expressed as the channel impulse response:

$$h(\tau) = \sum_{l=1}^L \alpha_l e^{j\phi_l} \delta(\varphi - \varphi_l) \quad (1)$$

where α_l , ϕ_l , and φ are the amplitude, phase, and time delay of the l -th multipath component, respectively; L indicates the total number of multipath components given in the channel; and $\delta(\phi)$ denotes the Dirac delta function.

B. Wi-Fi Sensing and Limitations

CSI patterns vary with human activity due to changes in wireless propagation, enabling activity and pose sensing via learning-based methods. However, modern Wi-Fi sensing systems increasingly offload high-rate CSI to the cloud, incurring significant communication overhead. For example, if a pair of Wi-Fi sensing devices operates on a 40MHz bandwidth (*i.e.* 114 subcarriers) with three pairs of antennas and a CSI sampling rate of 500Hz, the communication cost would be $3 \times 114 \times 500 \times 2 \times 4$ bytes/s (*i.e.*, 27.36Mb/s). To address this challenge, TinySense learns an effective compressed feature space for CSI data, bridging the gap between edge and cloud computing for large-scale Wi-Fi sensing.

C. VQ-VAE in Data Compression

VAE in [25] is a variant of an auto-encoder that presents the latent space Z by sampling from a simple distribution random variable. The training objective of VAE is to recover the true distribution of $p(x)$ rather than minimizing the reconstruction loss in the vanilla auto-encoder. Given a Gaussian prior assumption on z , the decoder $p(x | z)$ enables a straightforward factorization of the joint distribution as $p(x, z) = p(x | z)p(z)$. However, computing the marginal likelihood $p(x) = \int_z p(x | z)p(z)$ is typically intractable due to the large latent dimensionality. To address this, VAE framework optimizes the evidence lower bound (ELBO), which serves as a tractable surrogate objective for maximizing the data log-likelihood $p(x)$. The ELBO relies on an auxiliary distribution $q(z | x)$, referred to as the variational posterior. Its tightness relative to the true log-likelihood depends on how well $q(z | x)$ approximates the true posterior $p(z | x)$, with equality when the two distributions coincide. The VAE framework jointly trains the decoder distribution $p(x | z)$ and the encoder distribution $q(z | x)$ by maximizing the evidence lower bound (ELBO), defined as

$$\begin{aligned} \log p(x) &\geq \text{ELBO}(x) \\ &= \underbrace{\mathbb{E}_{q(z|x)} [\log p(x | z)]}_{\text{Distortion}} - \underbrace{D_{\text{KL}}(q(z | x) \| p(z))}_{\text{Rate}} \end{aligned} \quad (2)$$

where the distortion term corresponds to the reconstruction loss, while the rate term regularizes the latent representation by encouraging the variational posterior $q(z | x)$ to remain close to the prior $p(z)$. VQ-VAE [26] is a variant of the variational autoencoder [27] that employs discrete latent variables, even for continuous inputs. Owing to the fixed size and discrete nature of its latent code, VQ-VAE naturally lends itself to lossy compression. Consequently, it has been widely applied

in diverse compression tasks, including music generation and high-resolution image synthesis. In this work, we adopt VQ-VAE as the backbone for compressing CSI. By encoding CSI into discrete indices that are transmitted efficiently in binary form and reconstructed at the edge server, our approach benefits from both compactness and structural fidelity.

IV. METHODOLOGY

Our approach consists of *i*) an edge model at the local device and *ii*) a cloud model (see Fig. 2 (a)). By a dual selective kernel [20], an Encoder E at the local device extracts latent features \mathbf{Z} from the input CSI \mathbf{X} . These features are then compressed to reduce data size using a specified compression ratio η , with \mathbf{Z} mapped to VQ-indices \mathbf{I} through nearest-neighbor matching in a CSI codebook \mathbf{e}_k (Sec. IV-A) and inverted back to quantized vector \mathbf{Z}_q . The indices \mathbf{I} are further compressed into a bitstream using binary conversion before transmitting to the cloud. On the server, TinySense decompresses and reconstructs $\hat{\mathbf{Z}}_q$ by referencing the shared codebook \mathbf{e}_k to retrieve the corresponding codewords in matrix $\hat{\mathbf{I}}$, enabling two primary tasks: *i*) HPE via an Estimator E_s and *ii*) CSI reconstruction using Decoder G . For CSI data $\mathbf{X} \in \mathbb{R}^{F \times T \times C}$, where F , T , and C denote frequency, time, and channel, respectively, the compression pipeline includes five key components:

- **Encoder** $E(\cdot; \theta_E)$ transforms the input signal $\mathbf{X} \in \mathbb{R}^{F \times T \times C}$ into a latent representation $\mathbf{Z} \in \mathbb{R}^{\frac{F}{M} \times \frac{T}{M} \times D}$, where M and D are the reducing rate of encoder and the dimensionality of the latent codes, respectively.
- **Codebook** $\mathbf{e}_k \in \mathbb{R}^D, \forall k \in \{1, 2, \dots, K\}$ maps the latent representation \mathbf{Z} to a sequence of VQ indices \mathbf{I} and reconstructs it into a quantized version $\mathbf{Z}_q \in \mathbb{R}^{\frac{F}{M} \times \frac{T}{M} \times D}$ using the nearest neighbor lookup. A K-means clustering algorithm compresses the codebook to smaller subsets (see Fig. 2(b)).
- **Decoder** $G(\cdot; \theta_G)$ acts as a generator within the GAN framework, converting the quantized latent representation $\hat{\mathbf{Z}}_q$ back into reconstructed CSI data $\hat{\mathbf{X}} \in \mathbb{R}^{F \times T \times C}$.
- **Estimator** $E_s(\cdot; \theta_R)$ produces HPE based on the quantized latent representations $\hat{\mathbf{Z}}_q$.
- **Transformer** T predicts missing indices using the context of existing indices, as shown in Fig. 2 (c).

A. VQ-indices Compression

Unlike existing compression methods [28]–[32] that adopt scalar quantization, we integrate CNN inductive biases and principles from neural discrete representation learning [17].

VQ-indices process. Our model includes an encoder E and a decoder G that jointly represent CSI using codes from a learned discrete codebook \mathbf{e}_k . The codebook \mathbf{e}_k encodes the latent representation \mathbf{Z} by replacing each vector position with the index of the nearest vector in the codebook, based on Euclidean distance. This process produces a compressed latent representation with minimal loss of quality

$$I_{ij} = \underset{k \in 1, 2, \dots, K}{\operatorname{argmin}} \|\mathbf{Z}_{ij} - \mathbf{e}_k\| \quad (3)$$

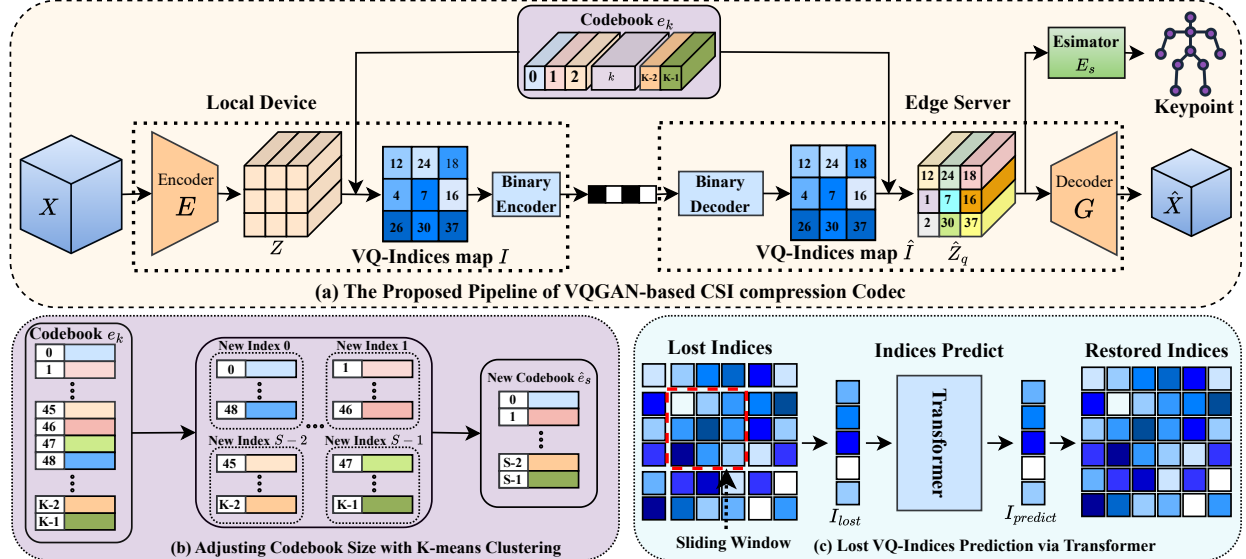


Fig. 2: Illustration of the proposed TinySense framework: (a) the overall compression pipeline, (b) the K-means clustering algorithm to adjust the codebook size for variable bitrates, and (c) a transformer approach for predicting lost VQ indices.

where i and j denote the positions of vector \mathbf{Z}_{ij} , with \mathbf{I}_{ij} representing the corresponding index. We obtain \mathbf{Z}_q through the quantization function $\mathbf{q}(\cdot)$, which assigns each element \mathbf{Z}_{ij} its index \mathbf{I}_{ij}

$$\mathbf{Z}_q = \mathbf{q}(\mathbf{Z}) = \{\mathbf{e}_k \mid \mathbf{I}_{ij}\} \in \mathbb{R}^{\frac{F}{M} \times \frac{T}{M} \times D}. \quad (4)$$

We then apply the Binary encoder to convert VQ indices (*i.e.*, decimal values) \mathbf{I} into bitstreams (*i.e.*, binary values) for transmission to the nearest server.

VQ loss function. After decoding, the reconstructed latent vectors $\hat{\mathbf{Z}}_q$ are generated by retrieving their corresponding code words based on their indices. The decoder G synthesizes the reconstructed CSI data $\hat{\mathbf{X}} \approx \mathbf{X}$ as

$$\hat{\mathbf{X}} = G(\mathbf{Z}_q) = G(\mathbf{q}(E(\mathbf{X}))). \quad (5)$$

Backpropagation through the non-differentiable quantization operation in (5) is managed with a straight-through gradient estimator. This allows gradients to flow from the decoder to the encoder [33] and enables end-to-end training of the model and codebook via the following loss function

$$\begin{aligned} \mathcal{L}_{\text{VQ}}(E, D, \hat{e}_s) = & \|\mathbf{X} - \hat{\mathbf{X}}\|_2^2 + \|\text{sg}[E(\mathbf{X})] - \mathbf{Z}_q\|^2 \\ & + \beta \|\text{sg}[\mathbf{Z}_q] - E(\mathbf{X})\|_2^2 \end{aligned} \quad (6)$$

where $\text{sg}[\cdot]$ indicates the stop-gradient operation, and $\|\text{sg}[\mathbf{Z}_q] - E(\mathbf{X})\|_2^2$ is the “*commitment loss*” with weighting factor β [34].

Adaptive compression via K-means. Codebook design is critical to compression efficiency. We implement a rate control strategy that adapts the compression bitrate by resizing the codebook using K-means clustering. Specifically, a large pretrained codebook is clustered to obtain centroids, which initialize smaller codebooks of varying sizes, each yielding a distinct set of VQ indices for compressed data representation.

This approach enables flexible codebook resizing while preserving quality. Specifically, the K-means algorithm begins

by randomly selecting centroids from the pre-trained large-scale codebook e_k . It then calculates the Euclidean distance between each codebook vector and the centroids, assigning each vector to the nearest centroid as follows

$$\mathbf{C}_s = \underset{s \in 1, 2, \dots, S}{\text{argmin}} \|\mathbf{e}_k - \hat{\mathbf{e}}_s\|^2 \quad (7)$$

where \mathbf{C}_s represents the s -th cluster, $\hat{\mathbf{e}}_s$ denotes the centroid of that cluster, and S (with $S < K$) denotes the new codebook size. Following this, the mean of the codebook vectors within each cluster C_j is recalculated, updating the cluster centroids accordingly as $\hat{\mathbf{e}}_s = \frac{1}{|C_s|} \sum_{\mathbf{e} \in C_s} \mathbf{e}$. These steps are repeated iteratively until the clustering minimizes the associated cost function

$$\min J(\mathbf{e}_k; \hat{\mathbf{e}}_s) = \min \left(\frac{1}{K} \sum_{k=1}^K \|\mathbf{e}_k - \hat{\mathbf{e}}_s\|^2 \right). \quad (8)$$

As a result, the newly created codebook $\hat{\mathbf{e}}_s$ from the K-means clustering algorithm can act as an initial point for further fine-tuning, accelerating convergence in the subsequent optimization process.

B. Learning Objective

Training Strategy. In addition to \mathcal{L}_{VQ} , we integrate VQGAN, an enhanced version of the original VQVAE, to incorporate adversarial loss and perceptual loss into the proposed approach. This integration is crucial for maintaining high perceptual quality, even at higher compression rates [17]. Specifically, we replace the L_2 loss in Eq. (6) with perceptual loss [35] and introduce a patch-based discriminator D , which uses adversarial training to differentiate between real and reconstructed CSI data, leading to

$$\mathcal{L}_{\text{GAN}}(\{E, G, \hat{e}_s\}, D) = [\log D(\mathbf{X}) + \log(1 - D(\hat{\mathbf{X}}))]. \quad (9)$$

Furthermore, TinySense aims to improve the accuracy of HPE tasks by employing the loss function that measures the

Algorithm 1 Training and Deployment of TinySense

Input: Labelled CSI data (\mathbf{X}, \mathbf{Y}), model weights $\theta_E, \theta_G, \theta_{E_s}$, CSI codebook \mathbf{e}_k , and number of iterations N_{iter} .

Initialize: Encoder E , decoder G , and estimator E_s with parameters θ_E, θ_G , and θ_{E_s} , respectively.

While $i \leq N_{\text{iter}}$ **do**

- 1) Input the labelled data (\mathbf{X}, \mathbf{Y});
- 2) Extract features \mathbf{Z} from \mathbf{X} using the encoder $E(\mathbf{X})$. Map \mathbf{Z} to VQ-indices map \mathbf{I} using codebook \mathbf{e}_k , and then retrieve quantized features \mathbf{Z}_q ;
- 3) Compress \mathbf{I} into a binary bitstream and transmit to the cloud;
- 4) Decompress the bitstream on the cloud side to retrieve the VQ-indices map $\hat{\mathbf{I}}$ by Binary Decoder;
- 5) Restore the quantized feature \mathbf{Z}_q from $\hat{\mathbf{I}}$;
- 6) Reconstruct CSI data $\hat{\mathbf{X}}$ using decoder G and predict results with estimator E_s ;
- 7) Update encoder θ_E and new codebook $\mathbf{e}_k := \mathbf{e}_s$ by solving (6) with K-means clustering;
- 8) Update θ_{E_s} and θ_G by minimizing (9) and (10).

▷ Deploy E at edge side, G and E_s at cloud server;
▷ Store the codebook \mathbf{e}_s on both sides.

distance between the predicted $\hat{\mathbf{Y}}$ and true label \mathbf{Y}

$$\mathcal{L}_{\text{keypoint}} = \|E_s(\hat{\mathbf{Z}}_q) - \mathbf{Y}\|_2^2 = \|\hat{\mathbf{Y}} - \mathbf{Y}\|_2^2. \quad (10)$$

Overall, our approach employs three primary objectives. \mathcal{L}_{VQ} , \mathcal{L}_{GAN} , and $\mathcal{L}_{\text{keypoint}}$. These objectives are strategically crafted to achieve the intended performance, as verified through extensive simulations.

Algorithm summary. We are now in a position to summarize the TinySense algorithm, providing a clear and accessible outline of the model optimization process. The objective is to find the optimal compression model $\mathcal{O}^* = \{E^*, G^*, E_s^*, \hat{\mathbf{e}}_s^*\}$:

$$\begin{aligned} \mathcal{O}^* = \arg \min_{E, G, \hat{\mathbf{e}}_s} \max_D \mathbb{E}_{x \sim p(x)} \left[\mathcal{L}_{\text{VQ}}(E, G, \hat{\mathbf{e}}_s) \right. \\ \left. + \lambda \mathcal{L}_{\text{GAN}}(\{E, G, \hat{\mathbf{e}}_s\}, D) + \mathcal{L}_{\text{keypoint}}(E_s) \right] \end{aligned} \quad (11)$$

where λ is calculated as

$$\lambda = \frac{\nabla_{G_L}[\mathcal{L}_{\text{rec}}]}{\nabla_{G_L}[\mathcal{L}_{\text{GAN}}] + \delta} \quad (12)$$

with \mathcal{L}_{rec} and $\nabla_{G_L}[\cdot]$ being the perceptual loss [36] and the gradient of the last layer L -th of the decoder, respectively. $\delta = 10^{-6}$ is used to maintain numerical stability. Specifically, we illustrate the TinySense training and deployment in Algorithm 1. Using existing CSI data, we first train the TinySense model offline, then deploy the feature extractor E at the local device, while the cloud server hosts the decoder G and Estimator E_s . The trained CSI codebook is stored on local devices and the server for compression and reconstruction.

C. Lost VQ-indices Prediction

Bitstream loss can lead to missing index information $\hat{\mathbf{I}}$, causing decoding errors. To mitigate this, we propose a generative transformer approach in the second stage of the proposed

model, aiming to predict missing indices during decoding to improve the fidelity of the reconstructed bitstream.

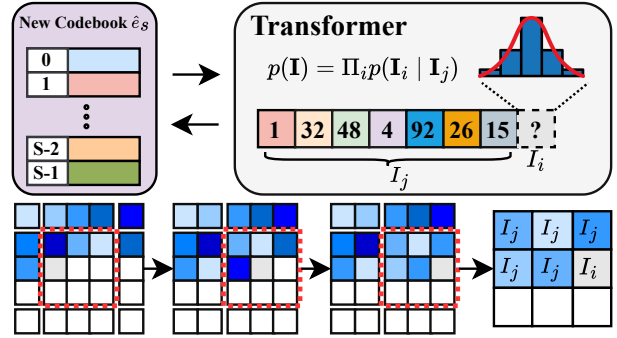


Fig. 3: The generative transformer process deployed in the second stage.

VQ-indices Transformer. As discussed in Sec. IV-A, the input CSI data \mathbf{X} can be represented by a map of the VQ indices \mathbf{I} , derived from its encodings. Specifically, the quantized representation of the CSI data \mathbf{X} is defined as $\mathbf{Z}_q = \mathbf{q}(E(\mathbf{X})) \in \mathbb{R}^{\frac{F}{M} \times \frac{T}{M} \times D}$, which corresponds to a sequence of indices $\mathbf{I} \in (1, \dots, S)^{\frac{F}{M} \times \frac{T}{M}}$ from the codebook. Each index is obtained by substituting the code with its corresponding index in the codebook \mathbf{e}_s

$$I_{ij} = k, \text{ such that } (\mathbf{Z}_q)_{ij} = \mathbf{Z}_k. \quad (13)$$

By mapping indices back to their respective entries in the codebook, the quantized features $\hat{\mathbf{Z}}_q = \hat{\mathbf{Z}}_{e_{ij}}$ can be easily reconstructed, and the CSI data is decoded as $\hat{\mathbf{X}} = G(\hat{\mathbf{Z}}_q)$.

Once an order is established for the indices in \mathbf{I} , the generation of CSI can be framed as an autoregressive prediction task of the next index. A second-stage transformer is trained to predict the probability distribution of each subsequent index $p(\mathbf{I}_i | \mathbf{I}_j)$ with $j < i$. The goal is to maximize the log-likelihood of the data representation, such as

$$\mathcal{L}_T = \mathbb{E}_{x \sim p(x)} [-\log p(\mathbf{I})] \quad (14)$$

where $p(\mathbf{I}) = \prod_i p(\mathbf{I}_i | \mathbf{I}_j)$. To simulate the potential loss of indices during transmission, we apply a binary mask $M = [m_i]_{i=1}^N$ as follows: If $m_i = 1$, the index \mathbf{I}_i is replaced by a special [mask] token to indicate its loss; if $m_i = 0$, \mathbf{I}_i remains unchanged. The mask ratio $\alpha \in [0, 1]$ controls the fraction of masked indices, denoted \mathbf{I}_{lost} as $\alpha \cdot N$. During the storage phase, as shown in Fig. 2 (c), the transformer predicts the probabilities of all potential codebook indices for each masked position i to allow reconstruction of lost indices.

Sliding window. To address the transformer's input sequence length limit N , we apply a sliding window approach, where a window of size $P \times P$ is centered on \mathbf{I}_i for each prediction, as illustrated in Fig. 3. Only indices j within this P -sized window are utilized as input, supporting the transformer's autoregressive function and aligning with the decoding process. This strategy improves the effective use of the spatial structure present in the CSI data. The predicted index $\hat{\mathbf{I}}_i$ is sampled and the reconstructed CSI data $\hat{\mathbf{X}}$ is generated by passing the predicted index sequence $\mathbf{I}_{\text{predict}}$ through the decoder G .

TABLE II: Compression Performance Comparison across Different Schemes on both MM-Fi and WiPose Datasets (“N/A” indicates methods not applicable to the task).

Method	η	MM-Fi				WiPose			
		NMSE (dB) ↓	PCK ₃₀ ↑	PCK ₂₀ ↑	MPJPE ↓	NMSE (dB) ↓	PCK ₁₀ ↑	PCK ₅ ↑	MPJPE ↓
LASSO	4	-8.42	N/A	N/A	N/A	-15.64	N/A	N/A	N/A
DeepCMC	4	-9.58	N/A	N/A	N/A	-16.86	N/A	N/A	N/A
GLC	4	-13.18	N/A	N/A	N/A	-20.75	N/A	N/A	N/A
CSINet	4	-4.75				-8.16			
	16	-4.25				-7.93			
	64	-4.05	N/A	N/A	N/A	-7.41	N/A	N/A	N/A
	128	-3.72				-6.98			
RCSNet	4	-13.02	55.14	42.62	170.15	-14.16	42.48	28.14	57.89
	16	-12.53	52.26	40.15	177.26	-14.06	37.12	23.69	64.13
	32	-12.36	49.24	36.72	186.18	-13.48	32.54	18.14	75.16
	64	-11.17	46.14	31.98	189.74	-13.35	23.17	12.68	88.17
EfficientFi	4	-14.94	62.15	48.01	166.62	-18.17	62.14	42.16	34.62
	16	-13.84	57.68	46.15	172.14	-17.58	59.73	38.96	40.18
	86	-13.26	52.47	40.68	178.18	-14.24	54.12	33.14	48.87
	570	-11.45	46.24	36.16	185.28	-11.36	46.95	26.89	62.14
	1710	-9.28	42.28	25.62	207.78	-7.07	34.18	15.39	86.16
	4	-15.14	66.16	51.93	156.72	-23.16	79.45	67.62	16.72
Ours	16	-14.82	64.24	48.59	163.21	-22.56	76.19	64.18	19.16
	86	-14.42	63.15	46.51	166.87	-22.12	70.82	59.89	25.47
	215	-13.74	60.89	41.21	170.98	-21.48	63.16	54.46	30.96
	570	-13.17	56.04	37.75	177.26	-21.01	54.96	45.39	38.42
	1710	-10.72	50.85	32.93	189.67	-18.16	42.19	36.72	50.58

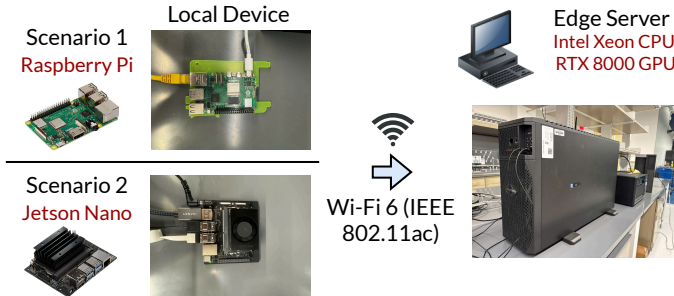


Fig. 4: Experimental setup for performance evaluation to evaluate the resource consumption.

V. EXPERIMENTAL EVALUATION

A. Experimental Settings

Datasets. We consider two datasets: MM-Fi [37] and Wi-Pose [6]. The MM-Fi dataset includes pose annotations with 17 skeleton points collected from a camera sensor and Wi-Fi CSI from 40 participants, covering 27 action categories across 14 daily activities and 13 rehabilitation exercises. In contrast, Wi-Pose provides pose annotations with 18 skeleton points and Wi-Fi CSI for 12 distinct actions performed by 12 volunteers, with data randomly split into training and testing sets.

Implementation details. The proposed approach and baselines are implemented in PyTorch and trained on a GeForce RTX 4070 for 50 epochs using the Adam optimizer, with a batch size of 128, a learning rate of 0.001, and a momentum of 0.9. To achieve the desired bitrate range, we apply K-Means clustering to reduce the codebook size, selecting from 2, 4, 8, 16, 32, 64, 128, 256, 512, 1024. The embedding dimen-

sion D is set to 256, and the weight λ is 0.5.

Baselines. We evaluate the effectiveness of our proposed TinySense by comparing it against six SOTA approaches: four basic CSI feedback models, including vanilla LASSO l_1 -solver [13], DeepCMC [38], CSINet [24], GLC [39], and two advanced compressive systems, RSCNet [15] and EfficientFi [14]. For HPE tasks, we benchmark against MetaFi++ [7], PerUnet [6], WiSPPN [5], PiW-3D [10], and AdaPose [9].

Criterion. For evaluation, we assess both CSI restoration quality and HPE task accuracy relative to the compression rate η . Restoration quality is measured using NMSE, which is quantified in decibels (dB) [14], [15]. For HPE task accuracy, we apply two common metrics: *i*) Percent Correct Keypoint (PCK) [40] and *ii*) MPJPE [40]. The original communication cost is 4 bytes per amplitude data point, totaling (total original data size) \times 4 bytes. In contrast, TinySense transmits only $K \log_2 K$ bytes, with K as the number of embeddings (*i.e.* codebook size of e_k), so the compression rate η is the ratio of the original cost to that of TinySense.

Real-world testbed setup and system deployment. As shown in Fig. 4, we set up two scenarios to evaluate resource consumption. In **Scenario 1**, we use a Raspberry Pi 5 as the mobile device and a Linux machine with an NVIDIA Quadro RTX 8000 GPU as the edge server. In **Scenario 2**, we replace the Raspberry Pi with a Jetson Nano, to represent a low-power edge AI device, while the server remains the same. To support real-time operation, we implement a double-buffering pipeline with buffers B_{current} and B_{next} , while Encoder E compresses data in B_{current} and B_{next} concurrently accumulates CSI packets ($T = 1$ s), preventing data acquisition stalls. Compressed indices are transmitted via TCP/IP, and the reported end-to-end

latency includes encoding, transmission, and decoding times, excluding cold-start buffering overhead.

B. Experimental Results

Compression task. We evaluate the compression performance of different schemes using NMSE, PCK_{20} , and MPJPE metrics. As shown in Table II, TinySense consistently outperforms LASSO, DeepCMC, CSINet, and GLC at the same compression rate of $\eta = 4$ and even achieves superior results at $\eta = 570$ with only a negligible increase in inference time on both MM-Fi and WiPose datasets. Compared to CSI-based sensing models like RCSNet and EfficientFi, TinySense also excels across all metrics. Notably, it achieves a PCK_{20} of 32.93% versus EfficientFi's 7.75% at $\eta = 1710$, while requiring less inference time. These results demonstrate that TinySense consistently surpasses SOTA models across both datasets.

TABLE III: HPE Tasks Performance Comparison Between Different Schemes on Both MM-Fi and WiPose Datasets (M: Million).

MM-Fi				
Method	η	$PCK_{20} \uparrow$	MPJPE \downarrow	Params \downarrow
WiSPPN	N/A	45.41	166.59	26.78M
PerUnet	N/A	52.12	154.66	34.51M
MetaFi++	N/A	48.64	162.45	26.42M
PiW-3D	N/A	52.18	155.69	16.47M
AdaPose	N/A	50.58	161.75	14.62M
	2	54.12	152.16	
Ours	4	51.93	156.72	1.66M
	16	48.59	163.21	
WiPose				
Method	η	$PCK_5 \uparrow$	MPJPE \downarrow	Params \downarrow
WiSPPN	N/A	52.95	32.37	26.33M
PerUnet	N/A	59.94	25.12	33.85M
MetaFi++	N/A	53.64	30.62	25.58M
PiW-3D	N/A	58.45	27.02	18.63M
AdaPose	N/A	55.12	28.84	16.25M
	8	65.36	17.75	
Ours	32	63.89	21.47	7.36M
	64	60.12	24.16	

HPE tasks. Table III compares TinySense with existing HPE methods. Focusing on relative pose accuracy, TinySense significantly outperforms SOTA, especially in low PCK_a and MPJPE, with low computational costs. PerUnet shows strong performance on both datasets, it does so at high complexity (34M parameters). Meanwhile, the two most recent methods, PiW-3D and AdaPose, demand significantly less computational resources than their counterparts but exhibit lower accuracy. Remarkably, at a compression rate of $\eta = 16$, TinySense achieves 48.59% in PCK_{20} , surpassing the performance of existing methods.

Lost VQ-indices prediction. To evaluate the generative transformer's effectiveness in recovering lost indices, we conduct simulations introducing varying error rates, denoted by ϵ , into the indices map $\hat{\mathbf{I}}$, with a fixed compression rate of 215 on MM-Fi dataset. We analyze performance trends across different error rates and compare the results to TinySense's

TABLE IV: Performance Comparison of TinySense with and without Transformer in the Presence of Lost Indices.

ϵ	TinySense			TinySense Without Transformer		
	NMSE \downarrow	$PCK_{20} \uparrow$	MPJPE \downarrow	NMSE	PCK_{20}	MPJPE
0.1	-12.02	39.16	171.45	-10.14	31.64	190.26
0.3	-11.24	36.12	178.63	-9.26	26.63	198.74
0.5	-10.88	32.69	186.54	-8.56	21.16	218.65
0.7	-10.04	30.14	192.68	-7.94	18.63	227.98
0.9	-9.65	26.89	198.86	-7.01	14.23	242.12

performance without the Transformer to highlight its impact on index recovery. As shown in Table IV, the model performance decreases as error rates increase; however, the reduction remains minimal, indicating that the Transformer effectively compensates for lost indices even at a high error rate of $\epsilon = 0.9$. In contrast, TinySense without the Transformer performs poorly even at low error rates, with a marked drop as ϵ rises to 0.9, achieving only around 14.23% in PCK_{20} .

C. Visualization Results

T-SNE visualization. We use t-SNE to show if similar features are clustered after compression, assessing the method's effectiveness. As shown in Fig. 5 (a), distinguishing different actions is challenging due to similar human pose patterns, complicating classification in HAR tasks. In contrast, the quantized features from TinySense in Fig. 5 (b) are distributed into distinct clusters within the compressed space, though the inherent similarity in poses prevents sharply defined boundaries typical of standard classification tasks. Similarly, for labeled subjects, the quantized features in Fig. 5(d) are more distinctly clustered, showing an improvement in Fig. 5(c).

Pose visualization. Fig. 6 presents qualitative results showcasing human skeleton visualizations at various compression rates from the MM-Fi dataset. Our approach focuses on generating 2D poses, which are then extended to 3D by adding a constant vector as the third dimension. The proposed TinySense method reliably produces accurate human poses at low compression rates and preserves pose integrity even under stringent compression conditions.

D. Ablation Study

TABLE V: Sensitivity Analysis of PCK_{20} (%) versus Embedding Dimension K and Weight Parameter λ on MM-Fi dataset: Best in **bold** and Second Best in underline.

Weight λ	$K = 64$	$K = 128$	$K = 256$	$K = 512$
0.10	36.8	41.8	46.5	44.1
0.25	40.5	42.1	44.3	43.6
0.50	41.8	<u>45.7</u>	41.5	39.3
0.75	39.7	42.6	39.6	42.6
1.00	37.5	42.5	41.5	43.3

Hyperparameter sensitivity. We investigate the effects of the embedding dimension K and the weight λ at a compression rate of $\eta = 86$, focusing on PCK_{20} accuracy. As illustrated in Table V, TinySense achieves peak performance with $K =$

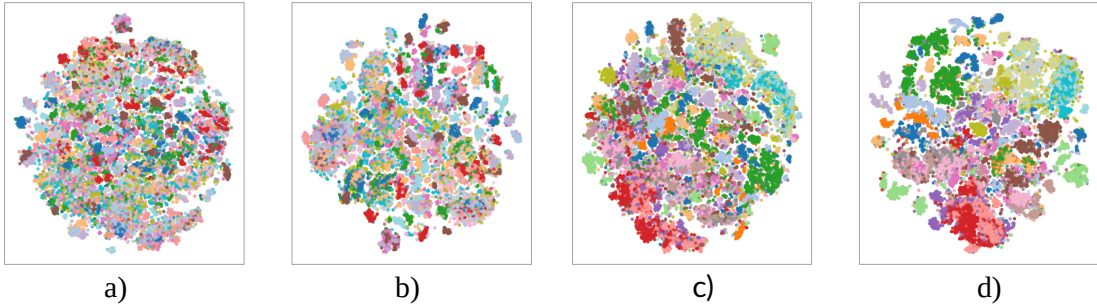


Fig. 5: T-SNE visualizations of CSI representations: (a) raw CSI with action labels, (b) quantized features with action labels, (c) raw CSI with subject labels, and (d) quantized features with subject labels.

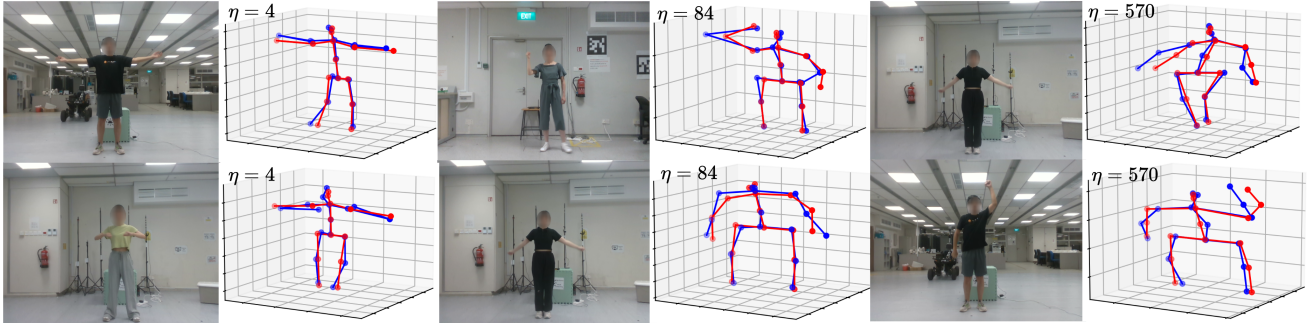


Fig. 6: Visualization of the human pose landmarks generated by the vision model (red) and Wi-Fi model (blue) on the MM-Fi at different compression rates.

128 and $\lambda = 0.5$, resulting in an accuracy of approximately 45%, and with $K = 256$ and $\lambda = 0.1$, reaching around 46.5%. The lowest accuracy occurs with $K = 64$, especially when $\lambda = 0.1$. Therefore, we adopt $K = 256$ and $\lambda = 0.1$ for all subsequent evaluations in this paper.

Impact of loss components. We conduct an ablation study on the MM-Fi dataset with $\eta = 215$ to evaluate the contribution of each loss term. As shown in Table VI, the full TinySense model using (11) achieves the best trade-off between reconstruction quality (NMSE) and pose accuracy (PCK₂₀). Removing \mathcal{L}_{GAN} results in a slight drop in PCK₂₀ while maintaining comparable NMSE. In contrast, ablating $\mathcal{L}_{keypoint}$ leads to a substantial degradation in sensing accuracy, despite a marginal NMSE improvement. This demonstrates that minimizing reconstruction error alone is insufficient, and $\mathcal{L}_{keypoint}$ is critical for preserving high-level semantic features required for HPE.

TABLE VI: Ablation Study of Loss Function Components ($\eta = 215$).

Configuration	NMSE \downarrow	PCK ₂₀ \uparrow	MPJPE \downarrow
Full TinySense	-13.74	41.21	170.98
w/o \mathcal{L}_{GAN}	-13.12	38.50	179.45
w/o $\mathcal{L}_{keypoint}$	-14.50	29.15	205.10

E. Analysis and Discussion

Integrated self-adaptive codebook with Transformer. We next simulate our approach, which incorporates a self-adaptive

TABLE VII: Assessment of TinySense Performance with Integrated Transformer and Adaptive Codebook Size Using K-means.

ϵ	η	NMSE \downarrow	PCK ₂₀ \uparrow	MPJPE \downarrow
0.1	215	-6.29	36.51	148.54
0.3	176	-6.44	36.78	148.52
0.5	96	-6.21	35.51	149.58
0.7	64	-5.51	35.78	149.73
0.9	16	-5.29	35.01	157.03

codebook using K-means clustering, with codebook sizes ranging from 16 to 128, while maintaining a threshold performance of PCK₂₀ $> 35\%$. As shown in Table VII, the compression rate η increases as the error rate ϵ decreases. However, the reduction in η is minimal when ϵ increases from 0.1 to 0.5, highlighting the effectiveness of the Transformer. In contrast, when ϵ reaches 0.9, the Transformer's performance diminishes, indicating that it is most effective at lower error rates.

TABLE VIII: Analysis of the Impact of the Transformer's Sliding Window on TinySense Performance.

P \times P	NMSE \downarrow	PCK ₃₀ \uparrow	PCK ₂₀ \uparrow	MPJPE \downarrow
2 \times 2	-13.782	60.152	39.086	170.45
3 \times 3	-14.422	63.158	46.516	166.87
4 \times 4	-13.582	59.238	40.562	172.69
5 \times 5	-14.082	62.881	44.163	168.14

Sliding window size. We investigate the effect of different sliding window sizes on model performance. Given the

sequence length constraints in the Transformer’s attention mechanism, we test window sizes of 2×2 , 3×3 , 4×4 , and 5×5 , with a fixed compression rate $\eta = 86$. As shown in Table VIII, performance initially improves as window size increases, then declines. The 2×2 window yields the lowest performance, while the optimal result of 166.87 mm is achieved with a 3×3 window. The second-best performance, 168.14 mm, is associated with 5×5 , with a minimal gap between 3×3 and 5×5 . Overall, the 3×3 window offers the best trade-off between accuracy and efficiency.

F. Resource Consumption on Testbed

We run experiments on a real-world testbed (see Fig. 4) under two deployment scenarios to measure end-to-end latency, energy consumption on local devices, and networking overhead. First, we conduct comparison experiments to assess the latency and networking overhead of our approach with its equivalent, including RCSNet [15] and EfficientFi [14], under the same performance. Furthermore, we implement a lightweight encoder-decoder architecture inspired by [20], which includes 10 DNN blocks. We evaluate three deployment strategies: **Local Computation (LC)**, where all computation runs on the local device; **Server-side Computation (SC)**, where raw data is sent to the server and all processing is done remotely; and **Edge-server Split (Ours)**, where the encoder (3 DNN blocks) runs locally and the rest runs on the server. In these experiments, we set $K = 128$ and $\lambda = 0.1$.

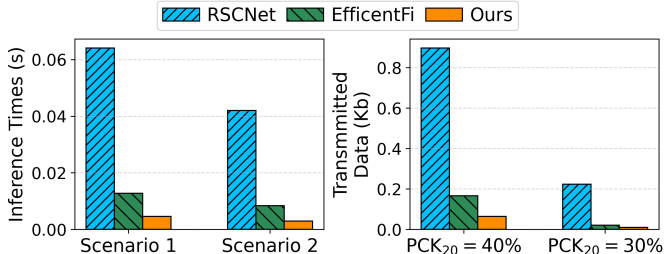


Fig. 7: Comparison of TinySense and baseline methods in terms of inference time (left) and network overhead (right).

Comparison to SOTA methods. Fig. 7 (left) shows that our approach reduces end-to-end inference latency by $14 \times$ and $5 \times$ compared with RCSNet [15] and EfficientFi [14], respectively, under the same accuracy level of $\text{PCK}_{20} = 40\%$ in Scenario 1. In Scenario 2, which involves a more powerful local device, TinySense also outperforms its counterparts, achieving an inference time of 3×10^{-3} s compared with 8×10^{-3} s and 4×10^{-2} s. These results demonstrate that our approach substantially reduces latency relative to existing CSI compression methods while maintaining the same accuracy. Fig. 7 (right) presents the bandwidth requirements of TinySense compared with RCSNet [15] and EfficientFi [14]. The results show that our method drastically reduces the transmission overhead. In particular, the transmitted data of TinySense is $14 \times$ and $5 \times$ smaller at $\text{PCK}_{20} = 40\%$, and $25 \times$ and $2.5 \times$ smaller at $\text{PCK}_{20} = 30\%$, compared with RCSNet

and EfficientFi, respectively. Overall, TinySense achieves remarkable improvements in both latency and transmission cost, highlighting its scalability and efficiency for real-world deployment.

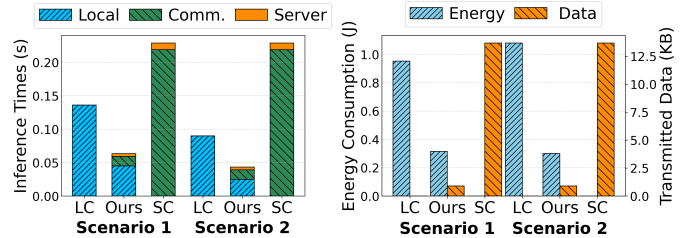


Fig. 8: Evaluation of the inference time (left), energy consumption, and networking overhead (right).

Comparison between employment strategies. As shown in Fig. 8 (left), TinySense achieves $2 \times$ and $3 \times$ lower inference latency compared to the LC and SC strategies, respectively, in Scenario 1. Notably, even when deployed on a more powerful local device, as in Scenario 2, TinySense still outperforms SC by approximately $4 \times$ in terms of latency. We further evaluate the trade-off between energy consumption on the local device and total transmitted data, as illustrated in Fig. 8 (right). The results demonstrate that TinySense strikes a favorable balance: it reduces local energy consumption by up to $3 \times$ compared to LC, while also lowering networking overhead by approximately $16 \times$ compared to SC in both scenarios. In general, TinySense attains the lowest end-to-end latency while simultaneously balancing energy efficiency and communication cost, highlighting its effectiveness as a Wi-Fi-based HPE solution under constrained communication, computation, and memory resources.

VI. CONCLUSION

This paper introduced TinySense, a compression framework that leverages a VQGAN to enhance the scalability of Wi-Fi-based human sensing. Our method achieves state-of-the-art accuracy and reconstruction quality, efficiently compressing original CSI data into lower-bit representations while requiring significantly less inference time compared to existing approaches. This success stems from the flexible integration of adaptive vector quantization with K-means and robust information recovery via a Transformer model. Through extensive validation on the MM-Fi and WiPose datasets, we have demonstrated TinySense’s robustness and generalizability across a wide range of challenging scenarios. These results pave the way for large-scale applications, especially on resource-constrained edge devices.

While TinySense performs robustly in single-person scenarios, future work will extend it to multi-user settings via source separation before quantization and address cross-domain adaptation using few-shot learning to update codebook centroids e_k with minimal retraining rapidly.

REFERENCES

[1] R. Zhou, M. Hao, X. Lu, M. Tang, and Y. Fu, "Device-free localization based on CSI fingerprints and deep neural networks," in *Proc. Annual IEEE Int. Conf. Sens., Commun., and Netw. (SECON)*, pp. 1–9, 2018.

[2] Z. Shi, Q. Cheng, J. A. Zhang, and R. Yi Da Xu, "Environment-robust wifi-based human activity recognition using enhanced CSI and deep learning," *IEEE Int. Things J.*, vol. 9, no. 24, pp. 24643–24654, 2022.

[3] Y. Zhao, R. Gao, S. Liu, L. Xie, J. Wu, H. Tu, and B. Chen, "Device-free secure interaction with hand gestures in WiFi-enabled IoT environment," *IEEE Int. Things J.*, vol. 8, no. 7, pp. 5619–5631, 2021.

[4] R. Che and H. Chen, "Channel state information based indoor fingerprinting localization," *Sensors (Basel, Switzerland)*, vol. 23, 2023.

[5] F. Wang *et al.*, "Can WiFi estimate person pose?," *Clini. Ortho. and Related Res. (CORR)*, vol. abs/1904.00277, 2019.

[6] Y. Zhou, A. Zhu, C. Xu, F. Hu, and Y. Li, "Perunet: Deep signal channel attention in unet for WiFi-based human pose estimation," *IEEE Sensors J.*, vol. 22, no. 20, pp. 19750–19760, 2022.

[7] Y. Zhou, H. Huang, S. Yuan, H. Zou, L. Xie, and J. Yang, "MetaFi++: WiFi-enabled transformer-based human pose estimation for metaverse avatar simulation," *IEEE Internet of Things J.*, vol. 10, no. 16, pp. 14128–14136, 2023.

[8] W. Jiang, H. Xue, C. Miao, S. Wang, S. Lin, C. Tian, S. Murali, H. Hu, Z. Sun, and L. Su, "Towards 3D human pose construction using WiFi," *Proc. Annul. Inter. Conf. Mobile Compu. and Netw.*, 2020.

[9] Y. Zhou, J. Yang, H. Huang, and L. Xie, "Adapose: Toward cross-site device-free human pose estimation with commodity wifi," *IEEE Int. Things J.*, vol. 11, no. 24, pp. 40255–40267, 2024.

[10] K. Yan, F. Wang, B. Qian, H. Ding, J. Han, and X. Wei, "Person-in-wifi 3d: End-to-end multi-person 3d pose estimation with wi-fi," in *Proc. IEEE/CVF Conf. Comput. Vision and Patt.n Recog. (CVPR)*, pp. 969–978, June 2024.

[11] K. P. F.R.S., "Liii. on lines and planes of closest fit to systems of points in space," *Philosophical Magazine Series 1*, vol. 2, pp. 559–572, 1901.

[12] C. Eckart and G. M. Young, "The approximation of one matrix by another of lower rank," *Psychometrika*, vol. 1, pp. 211–218, 1936.

[13] I. Daubechies, M. Defrise, and C. D. Mol, "An iterative thresholding algorithm for linear inverse problems with a sparsity constraint," *Communications on Pure and Applied Mathematics*, vol. 57, 2003.

[14] J. Yang, X. Chen, H. Zou, D. Wang, Q. Xu, and L. Xie, "EfficientFi: Toward large-scale lightweight WiFi sensing via CSI compression," *IEEE Int. Things J.*, vol. 9, no. 15, pp. 13086–13095, 2022.

[15] B. Barahimi, H. Singh, H. Tabassum, O. Waqar, and M. Omer, "RSCNet: Dynamic CSI compression for cloud-based WiFi sensing," in *Proc. IEEE Int. Conf. Commun.*, pp. 4179–4184, 2024.

[16] S. Tang, J. Xia, L. Fan, X. Lei, W. Xu, and A. Nallanathan, "Dilated convolution based CSI feedback compression for massive MIMO systems," *IEEE Transactions on Vehicular Technology*, vol. 71, no. 10, pp. 11216–11221, 2022.

[17] P. Esser, R. Rombach, and B. Ommer, "Taming transformers for high-resolution image synthesis," *Proc. IEEE/CVF Conf. Comput. Vision and Patt.n Recog. (CVPR)*, pp. 12868–12878, 2020.

[18] L. Guo, Z. Lu, X. Wen, S. Zhou, and Z. Han, "From signal to image: Capturing fine-grained human poses with commodity WiFi," *IEEE Commun. Lett.*, vol. 24, no. 4, pp. 802–806, 2020.

[19] J. Yang, Y. Zhou, H. Huang, H. Zou, and L. Xie, "MetaFi: Device-free pose estimation via commodity WiFi for metaverse avatar simulation," in *IEEE 8th World Int. of Things (WF-IoT)*, pp. 1–6, 2022.

[20] T. D. Gian, T. Dac Lai, T. Van Luong, K.-S. Wong, and V.-D. Nguyen, "Hpe-li: WiFi-enabled lightweight dual selective kernel convolution for human pose estimation," in *Euro. Conf. Comput. Vision (ECCV)*, (Berlin, Heidelberg), p. 93–111, Springer-Verlag, 2024.

[21] X. Hoang Nguyen, V.-D. Nguyen, Q.-T. Luu, T. Dinh Gian, and O.-S. Shin, "Robust wifi sensing-based human pose estimation using denoising autoencoder and cnn with dynamic subcarrier attention," *IEEE Internet of Things Journal*, vol. 12, no. 11, pp. 17066–17079, 2025.

[22] T. D. Gian, D. T. Tran, Q.-V. Pham, L.-N. Tran, and V.-D. Nguyen, "Multi-modal human pose estimation: A wi-fi-driven approach with adaptive kernel selection," *IEEE Transactions on Artificial Intelligence*, pp. 1–14, 2025.

[23] T. D. Gian, T.-H. Nguyen, N. T. Nguyen, and V.-D. Nguyen, "Wilhpe: WiFi-enabled lightweight channel frequency dynamic convolution for hpe tasks," in *2024 Tenth International Conference on Communications and Electronics (ICCE)*, pp. 516–521, 2024.

[24] M. B. Mashhadi, Q. Yang, and D. Gündüz, "Distributed deep convolutional compression for massive MIMO CSI feedback," *IEEE Trans. Wireless Commun.*, vol. 20, no. 4, pp. 2621–2633, 2021.

[25] D. P. Kingma and M. Welling, "Auto-encoding variational bayes," *arXiv preprint arXiv:1312.6114*, 2013.

[26] A. van den Oord, O. Vinyals, and K. Kavukcuoglu, "Neural discrete representation learning," *ArXiv*, vol. abs/1711.00937, 2017.

[27] D. J. Rezende, S. Mohamed, and D. Wierstra, "Stochastic backpropagation and approximate inference in deep generative models," in *International conference on machine learning*, pp. 1278–1286, PMLR, 2014.

[28] Z. Cheng, H. Sun, M. Takeuchi, and J. Katto, "Learned image compression with discretized gaussian mixture likelihoods and attention modules," *Proc. IEEE/CVF Conf. Comput. Vision and Patt.n Recog. (CVPR)*, pp. 7936–7945, 2020.

[29] L. Theis, W. Shi, A. Cunningham, and F. Huszár, "Lossy image compression with compressive autoencoders," *ArXiv*, vol. abs/1703.00395, 2017.

[30] Y. Choi, M. El-Khamy, and J. Lee, "Variable rate deep image compression with a conditional autoencoder," in *Proc. IEEE/CVF Int. Conf. Comput. Vision (ICCV)*, pp. 3146–3154, 2019.

[31] F. Yang, L. Herranz, J. v. d. Weijer, J. A. I. Gutián, A. M. López, and M. G. Mozerov, "Variable rate deep image compression with modulated autoencoder," *IEEE Signal Processing Letters*, vol. 27, pp. 331–335, 2020.

[32] C. Gao, T. Xu, D. He, H. Qin, and Y. Wang, "Flexible neural image compression via code editing," *ArXiv*, vol. abs/2209.09244, 2022.

[33] Y. Bengio, "Estimating or propagating gradients through stochastic neurons," *ArXiv*, vol. abs/1305.2982, 2013.

[34] A. van den Oord, O. Vinyals, and K. Kavukcuoglu, "Neural discrete representation learning," in *Proceedings of the 31st International Conference on Neural Information Processing Systems*, NIPS'17, (Red Hook, NY, USA), p. 6309–6318, Curran Associates Inc., 2017.

[35] J. Johnson, A. Alahi, and L. Fei-Fei, "Perceptual losses for real-time style transfer and super-resolution," in *Euro. Conf. Comput. Vision (ECCV)*, (Cham), pp. 694–711, Springer International Publishing, 2016.

[36] R. Zhang, P. Isola, A. A. Efros, E. Shechtman, and O. Wang, "The unreasonable effectiveness of deep features as a perceptual metric," *Proc. IEEE/CVF Conference on Computer Vision and Pattern Recognition*, pp. 586–595, 2018.

[37] J. Yang, H. Huang, Y. Zhou, X. Chen, Y. Xu, S. Yuan, H. Zou, C. X. Lu, and L. Xie, "MM-Fi: Multi-modal non-intrusive 4D human dataset for versatile wireless sensing," in *Thirty-seventh Conf. Neural Infor. Process. Sys. Data. and Bench. Track*, 2023.

[38] M. B. Mashhadi, Q. Yang, and D. Gündüz, "Distributed deep convolutional compression for massive MIMO CSI feedback," *IEEE Trans. Wire. Commun.*, vol. 20, no. 4, pp. 2621–2633, 2021.

[39] Z. Jia, J. Li, B. Li, H. Li, and Y. Lu, "Generative latent coding for ultra-low bitrate image compression," in *Proc. IEEE/CVF Conf. Comput. Vision and Patt.n Recog. (CVPR)*, pp. 26088–26098, 2024.

[40] J. Wang, S. Tan, X. Zhen, S. Xu, F. Zheng, Z. He, and L. Shao, "Deep 3D human pose estimation: A review," *Computer Vision and Image Understanding*, vol. 210, p. 103225, 2021.